RSC Advances

PAPER

View Article Online
View Journal | View Issue

Cite this: *RSC Adv.*, 2020, **10**, 27538

2D black phosphorus and tungsten trioxide heterojunction for enhancing photocatalytic performance in visible light

Qi Wang,[a] Bihan Li,[b] Ping Zhang,[a] Wenming Zhang,[c] Xiaoru Hu[a] and Xiaochen Li *[a]

Received 14th June 2020
Accepted 13th July 2020

DOI: 10.1039/d0ra05230b

rsc.li/rsc-advances

A novel, efficient and stable 2D black phosphorus and tungsten trioxide heterojunction (WO_3–BPNs) was successfully synthesized using a combined hydrothermal, liquid phase exfoliating and co-precipitation method. The as-obtained WO_3–BPNs composite was characterized by using XRD, SEM, XPS, UV-vis, *etc.* The results showed that the bandgap energy of the WO_3–BPNs50 sample was 2.2 eV, which was lower than that of pure WO_3. BPNs in the WO_3–BPNs heterojunction as a co-catalyst effectively enhanced photo-generated electron–hole pairs separation. The synthesized WO_3–BPNs sample significantly improved the photocatalytic performance in degrading rhodamine B (RhB) and metoprolol (MET) compared to pure WO_3 and BPNs under visible-light. The maximum RhB and MET removal efficiencies were 92% and 87%, respectively, in the WO_3–BPNs50 (added 50 mL BPNs dispersion) sample within 120 minutes. The relevant photocatalysis mechanisms were discussed. In addition, the intermediate products in the MET photodegradation process were investigated by LC-MS technology, and the degradation pathway of MET was proposed.

1 Introduction

Recently, a large number of toxic and hazardous organic pollutants have been released into aquatic environments, creating more and more environmental concerns.[1,2] The photodegradation of organic contaminants under solar radiation using semiconductor materials has been considered as a promising method for treating such pollutants.[3] Many semiconductor materials such as TiO_2,[4] WO_3,[5] ZnO,[6] and CdS[7] have been extensively investigated as photocatalysts for degrading organic pollutants under solar radiation. However, the low utilization rate of visible-light and the rapid recombination of photoelectron–hole pairs under photodegradation still inhibit the practical applications of semiconductor photocatalysts in the treatment of organic pollutants.[1,2]

Many investigations have been conducted to overcome these disadvantages and improve the photocatalytic performance, mainly including ion doping and the formation of heterojunction structures between two semiconductor materials.[5,8] Previous studies demonstrated that photocatalytic performance of semiconductor materials was significantly enhanced due to the doping of non-metal elements N,[9] S,[5] and P,[10] or metal elements Cu,[11] Ag,[12] and Ce.[13] Liang *et al.* proposed that Ag/TiO_2 and Ce/TiO_2 have high photocatalytic degradation performance for formaldehyde gas under UV-light.[13] The photocatalytic performance of catalyst can also be effectively improved by preparing a heterojunction structure between two semiconductor materials.[8] The formation of a heterojunction structure between two different semiconductors could broaden the spectral response range and reduce the recombination of photogenerated carriers.[14] Gao *et al.* found that the photodegradation efficiency promoted for the WO_3/TiO_2 heterojunction photocatalyst compared to WO_3 and TiO_2 under visible-light.[8] More importantly, two-dimensional (2D) semiconductor materials attract extensive attentions benefiting from high charge-carrier mobility and adjustable bandgap energy.[14] Ali *et al.* reported the graphene–TiO_2 nanocomposites to enhance the photodegradation of rhodamine B dye.[15] Kanda *et al.* prepared MoS_2–TiO_2 nanocomposite using a photo deposition-based technique for improving photocatalytic performance.[16] However, the zero band gap of graphene[17] and the low carrier mobility of MoS_2 ($200\ cm^2\ V^{-1}\ s^{-1}$)[18] limited their further development in the field of optoelectronics.

Black phosphorus (BP) has been recently attracted considerable attention due to its unique in-plane anisotropic structure, high carrier mobility, and adjustable direct bandgap.[19,20] The adjustable direct bandgap of BP mainly depends on the exfoliation of BP layers, for instance the bandgap energy of bulk and single-layer BP is 0.3 eV and 1.5 eV, respectively.[21,22] Thus, it is possible to expand the spectrum response of BP to

---

[a] College of Water Conservancy and Civil Engineering, Shandong Agricultural University, Tai'an, Shandong 271018, PR China. E-mail: lixiaochen02@163.com

[b] College of Life Science, Shandong Agricultural University, Tai'an, Shandong 271018, PR China

[c] Department of Civil and Environmental Engineering, Donadeo Innovation Centre for Engineering, University of Alberta, Edmonton, Alberta, Canada

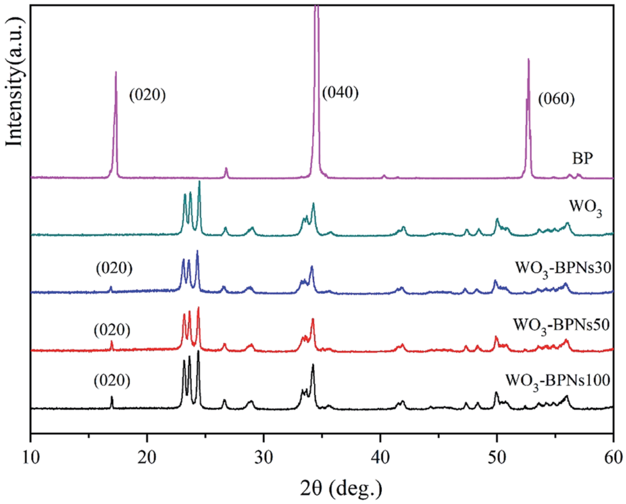

Fig. 1 XRD patterns of bulk BP, WO_3 and WO_3–BPNs composites.

visible, mid-infrared and near-infrared light by controlling the thickness of BP. Lee *et al.* reported BP@TiO_2 photocatalysts had excellent photocatalytic performance under sunlight and little effect on temperature and pH conditions.[23] Hu *et al.* prepared a heterojunction structure of 2D/2D BP/monolayer Bi_2WO_6 to improve the photocatalytic performance to produce H_2.[24] A BP–Au/LTO nanostructure prepared by Majima *et al.* was proved to be a high-efficiency photocatalyst for generating hydrogen under visible-light.[25] In fact, despite BP has excellent optoelectronic properties, its photocatalytic performance remains largely unexplored in the application of degrading organic pollutants in aquatic environments under both UV and visible-lights.

In this study, a novel heterojunction of two-dimensional black phosphorus and WO_3 (WO_3–BPNs) was synthesized using a combined method of hydrothermal, liquid phase exfoliating and co-precipitation for the first time. The as-obtained WO_3–BPNs composite was characterized by using X-ray diffraction (XRD), scanning electron microscopy (SEM), atomic force microscopy (AFM), X-ray photoelectron spectroscopy (XPS), specific surface aperture analysis (BET) and diffuse reflectance spectroscopy (UV-vis). The photocatalytic performance of the prepared WO_3–BPNs was evaluated with rhodamine B (RhB) and metoprolol (MET) degradation experiments under visible-light. The photocatalysis mechanisms were also revealed and discussed. Finally, MET was selected to study the intermediate products in the photodegradation process with LC-MS technique, and a scheme of MET degradation pathway had been proposed.

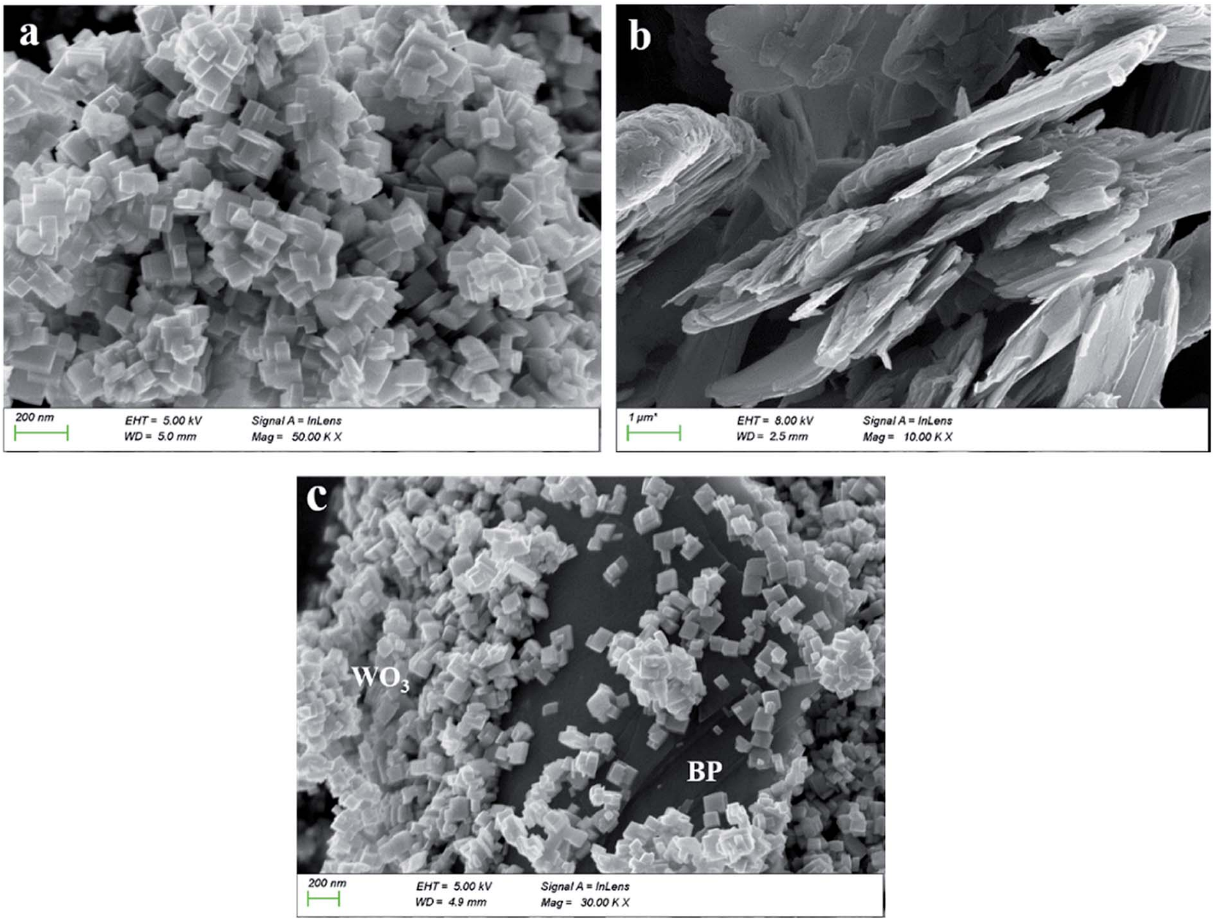

Fig. 2 SEM images of WO_3 (a), BPNs (b) and WO_3–BPNs50 composites (c).

2 Materials and methods

2.1 Chemicals

The BP crystals were supplied by Kunming Black Phosphorus Technology Co., Ltd. Rhodamine B (RhB) and *N*-methyl-2-pyrrolidone (NMP) (≥99.0%) were supplied by Shanghai Aladdin Biochemical Technology Co., Ltd. Metoprolol tartrate salt (≥98.0%) supplied by Shanghai Macklin Biochemical Co., Ltd. $Na_2WO_4 \cdot 2H_2O$ and NaOH were supplied by Tianjin Yongda Chemical Reagent Co., Ltd.

2.2 Sample preparation

2.2.1 Preparation of the monoclinic WO_3 nanocrystals and BP nanosheets. Monoclinic WO_3 was synthesized with a hydrothermal method. First, 1.1547 g $Na_2WO_4 \cdot 2H_2O$ was dispersed in 60 mL deionized water, and 35 mL HCl was mixed into the above-mixed solution. Then, the mixture had been placed in

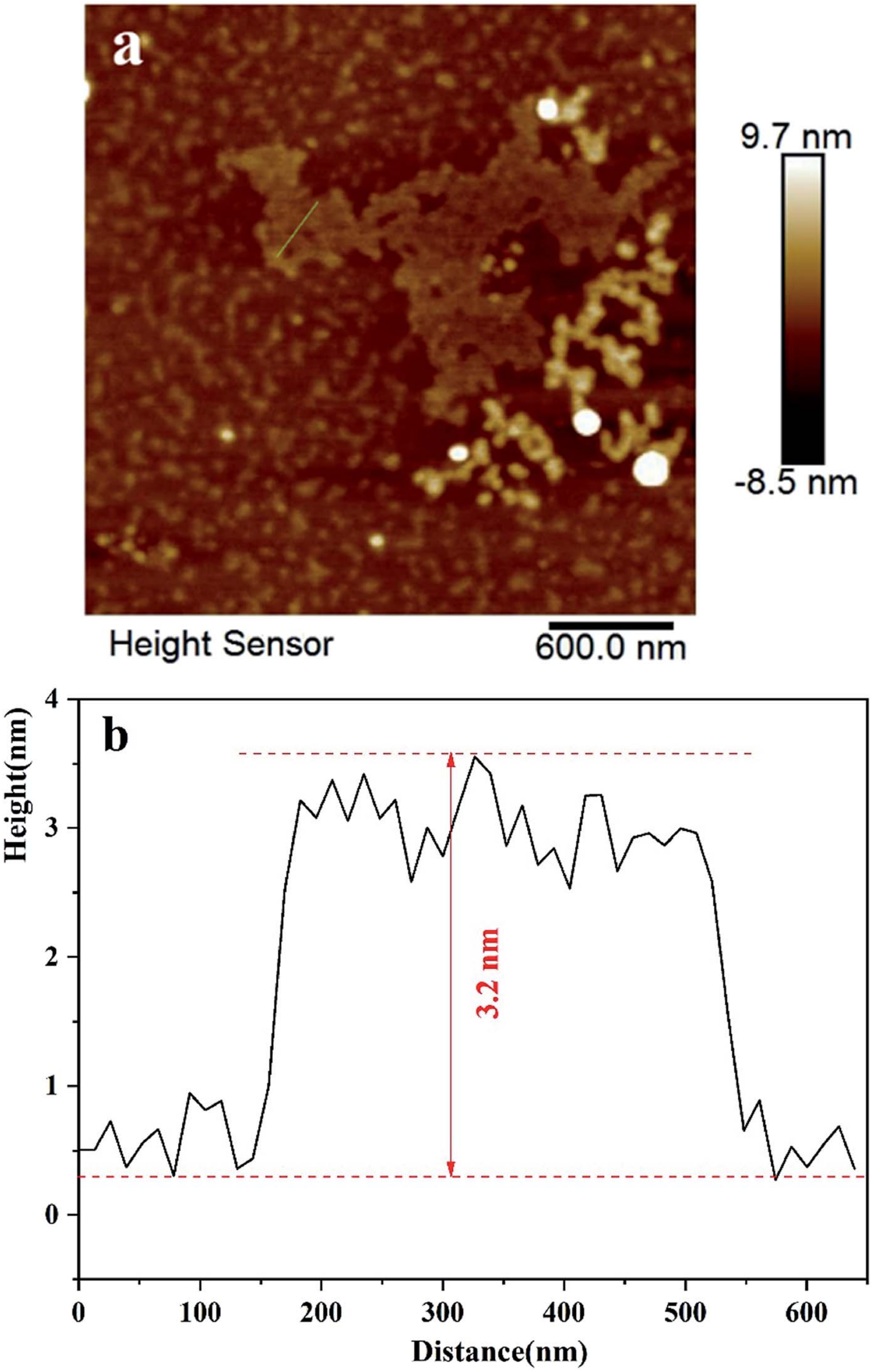

Fig. 3 AFM images (a) and 1D cross-sectional scan of surface profile thickness of the BPNs sample (b).

a stainless steel autoclave lined with Teflon and kept at 180 °C for 12 h. Finally, the hydrothermal product was repeatedly washed with deionized water and dried for further use.

The BP nanosheets (BPNs) were obtained by solvent exfoliation process. Finally, 30 mg bulk BP was ground into the powder with an agate mortar. The BP powder was dispersed into

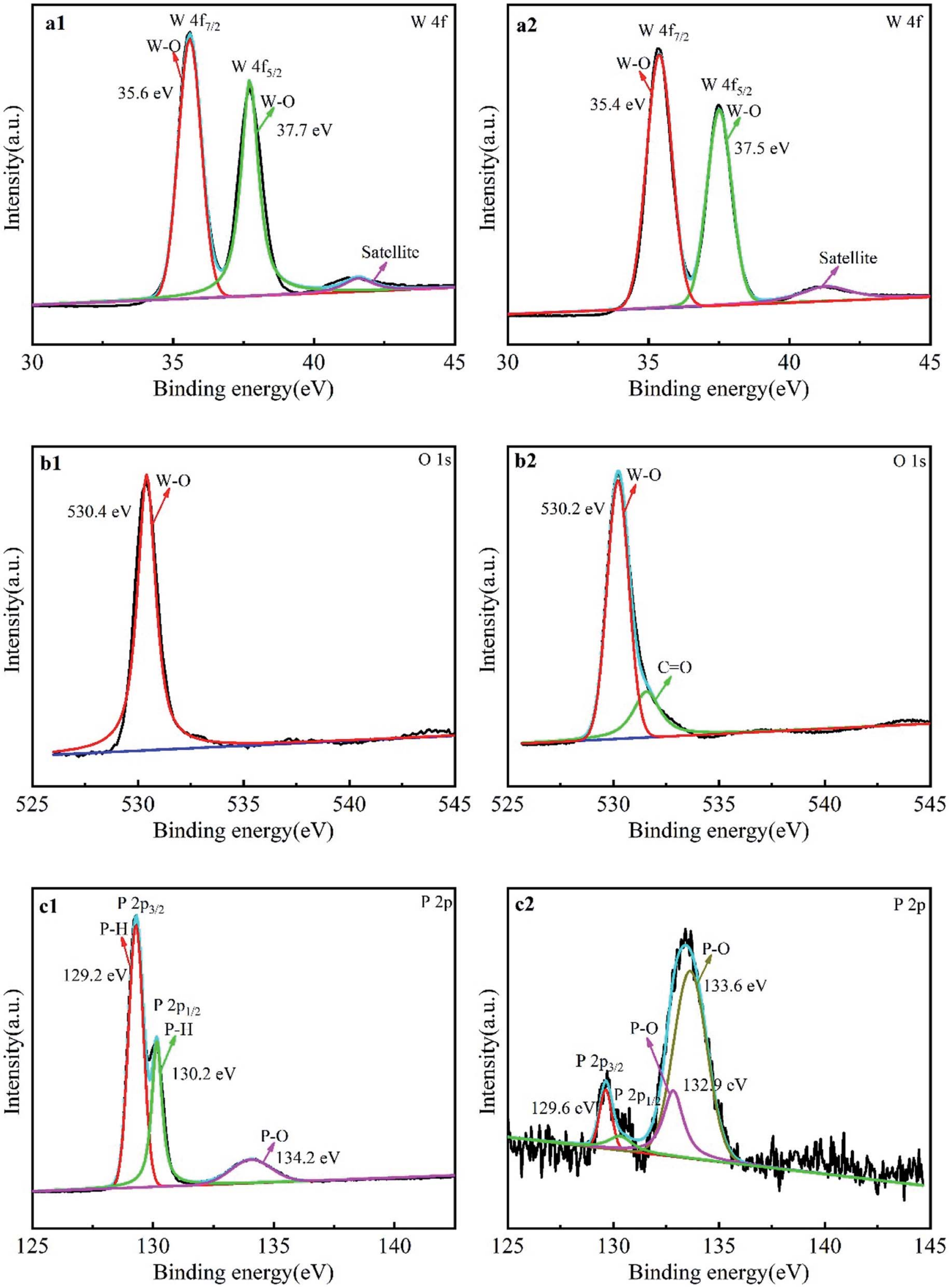

Fig. 4 XPS spectra for W 4f of WO_3 (a1) and WO_3–BPNs50 (a2), O 1s of WO_3 (b1) and WO_3–BPNs (b2), and P 2p of BP (c1) and WO_3–BPNs (c2).

80 mL NMP solution, then added 10 mg NaOH. The dispersion was sonicated in an ice bath for 6 hours, and the output power of the sonicator was 300 W. The non-exfoliated bulk BP was removed from the obtained dispersion solution by centrifugation at 2000 rpm for 20 minutes. Then the supernatant after centrifugation was sonicated in an ice bath for 2 hours and the BP quantum dot had been removed though centrifugation at 7000 rpm for 20 minutes to obtain the BPNs. The product was resuspended in 30 mL NMP solution for further use. The concentration of BPNs dispersion was 0.2 mg mL^{-1}.

2.2.2 Preparation of the WO$_3$–BPNs sample. The WO$_3$–BPNs sample was synthesized by co-precipitation in aqueous solution. In detail, 231.84 mg monoclinic WO$_3$ was added to the 30 mL, 50 mL, and 100 mL BPNs dispersion (0.2 mg mL^{-1}), which were marked as WO$_3$–BPNs30, WO$_3$–BPNs50, WO$_3$–BPNs100 respectively. WO$_3$ and BPNs dispersion were stirred for 2 hours and ultrasonicated for another 2 hours. The product was collected from the dispersion by high-speed centrifugation (7000 rpm). The product was sufficiently washed with deionized water to neutrality. Finally, the WO$_3$–BPNs sample was obtained by freeze-dried.

2.3 Characterization

The analysis of the crystal structure of the obtained sample was performed by XRD at 20 °C using an X-ray diffractometer (D8-Advance), and the diffraction angle ranged from 10° to 60°. The morphology of the obtained sample was characterized by using an SEM (sigma 300 SEM, Japan), with scanning voltage of 8 and 5 kV for BP and other samples. The binding energy was analyzed by an XPS (Thermo ESCALAB 250XI, Japan). The thickness of BP nanosheet was analyzed with AFM images (Bruker Dimension Edge). The UV-vis diffuse reflectance spectra were tested using a UV-2450 with an integrating sphere (ISR-240, Japan).

2.4 Photocatalytic performance experiments

The photocatalytic efficiency of WO$_3$–BPNs samples were tested by photodegrading RhB and MET with visible-light. The 350 W Xe-lamp (1900 mW cm^{-2}) was used in the photocatalysis experiment as the light source. The Xe-lamp was equipped with a 420 nm cut-off filter to eliminate the effect of ultraviolet light. The sample (50 mg WO$_3$–BPNs) was added into a quartz tube with 50 mL RhB (10 mg L^{-1}) or MET (10 mg L^{-1}). The solution was placed without light for 30 minutes to achieve the equilibrium of adsorption and desorption. The 5 mL mixed solution was taken every 30 minutes for testing, and the suspended photocatalyst was removed though centrifugation. The concentrations of RhB and MET solution were evaluated utilizing a UV-vis spectrophotometer (UV-2450) and a high-efficiency liquid chromatography (Shimadzu, LC-10AT, Japan), respectively.

2.5 Analysis of metoprolol and its degradation products

MET and its oxidation by-products were identified by using the Ultimate 3000 UHPLC-Q Exactive LC/MS (Thermo Scientific, US) with Eclipse Plus C18 column, 250 × 4.6 mm during the photoreaction. The mobile phase used in the test was a 0.1% mixture of formic acid and acetonitrile with the volume ratio of 20 : 80. The device measurement mode was positive ion mode, using ESI ion source, the range: 50–750 m/z; the flow rate: 0.4 mL min^{-1}; DL tube temperature: 300 °C; gas lift rate: 40 mL min^{-1}; auxiliary gas rate: 10 mL min^{-1}; spray voltage: positive ion 4.0 kV; and fragmentation energy: NCE 30.

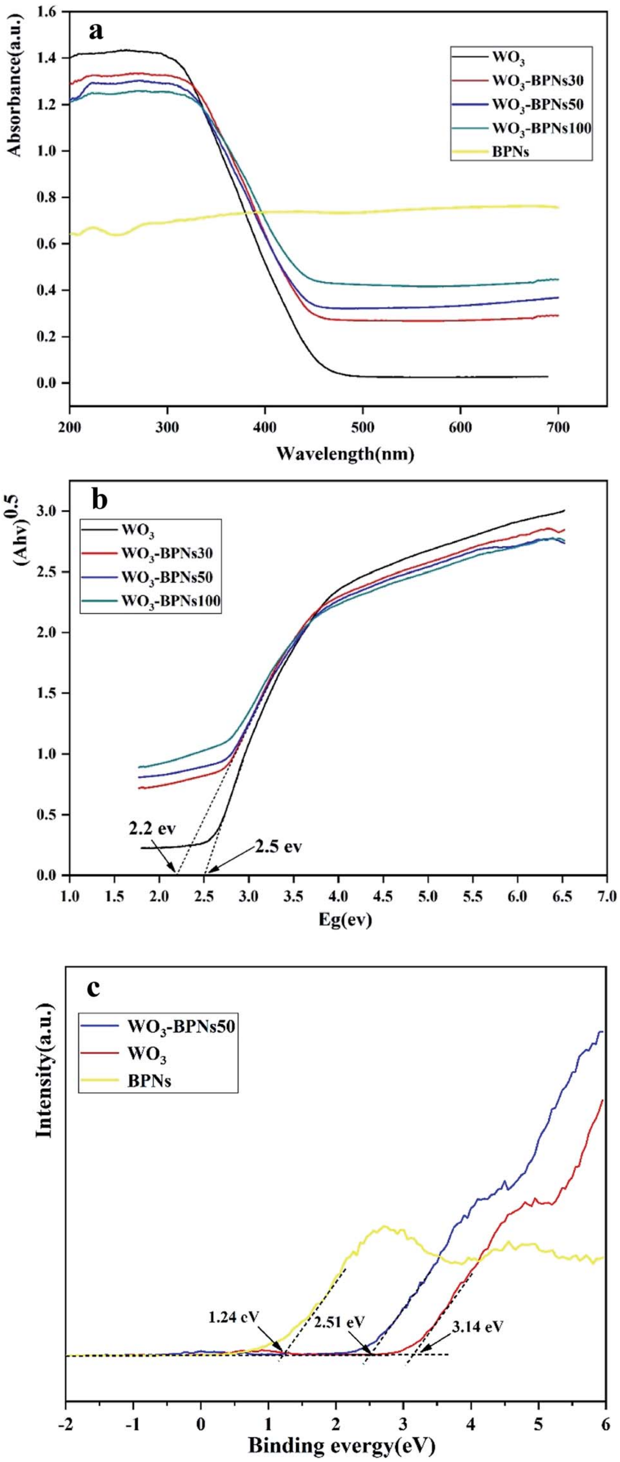

Fig. 5 UV-vis diffuse reflectance spectra of WO$_3$ and WO$_3$–BPNs (a), and plot of the $(\alpha h\nu)^{0.5}$ *versus* $h\nu$ (b), VBXPS spectra of WO$_3$, BPNs and WO$_3$–BPNs50 (c).

3 Results and discussions

3.1 Characterization of the WO_3–BPNs sample

3.1.1 Structural and morphological analysis. The XRD patterns of bulk BP, WO_3, and WO_3–BPN were depicted in Fig. 1. It could be detected clearly that the characteristic diffraction peaks of the obtained WO_3 and bulk BP match well with the monoclinic WO_3 crystal structure (JCPDS card no. 043-1035) and BP crystal structure (JCPDS card no. 76-1957). The diffraction peaks at 17.3°, 34.6° and 52.7° were assigned to the (020), (040) and (060) planes of BP, respectively.[23] The diffraction peaks at 23.1°, 23.6°, 24.4°, and 26.6° were assigned to the (002), (020), (200) and (120) planes of the monoclinic WO_3, respectively.[26] All the diffraction peaks of WO_3–BPNs composite can be ascribed to WO_3 and bulk BP, without any other peaks. In addition, the diffraction peaks of the composite samples were very similar to those of pure WO_3, indicating that the intervention of BPNs had little effect on the lattice parameters of WO_3. The intensity of the diffraction peak of the (020) crystal plane also increased with the increase of the amount of BPNs doping.

Fig. 2a–c show SEM images of WO_3, BP and WO_3–BPNs, respectively. In Fig. 2a, WO_3 nanoparticles are 50–100 nm in

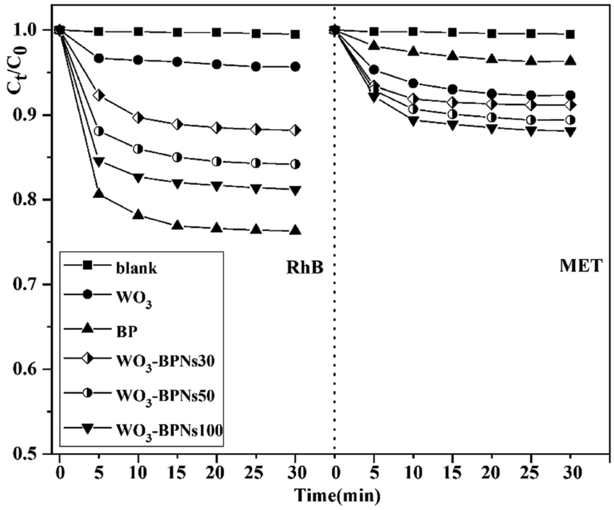

Fig. 6 Adsorption of RhB and MET by all samples.

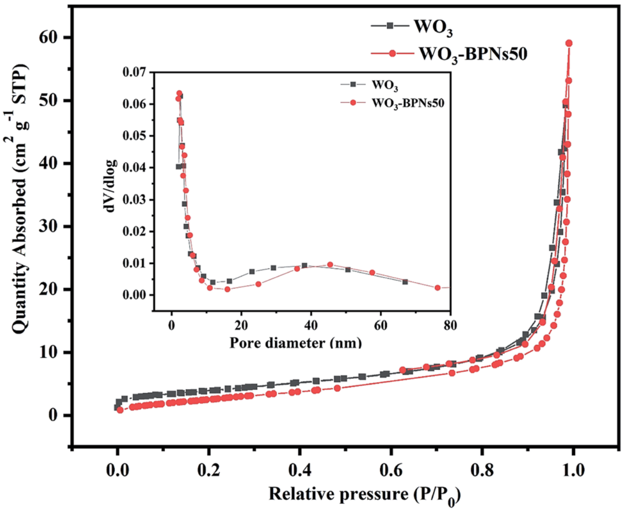

Fig. 7 N_2 absorption–desorption isotherms and corresponding pore-size distribution curves for WO_3 and WO_3–BPNs50.

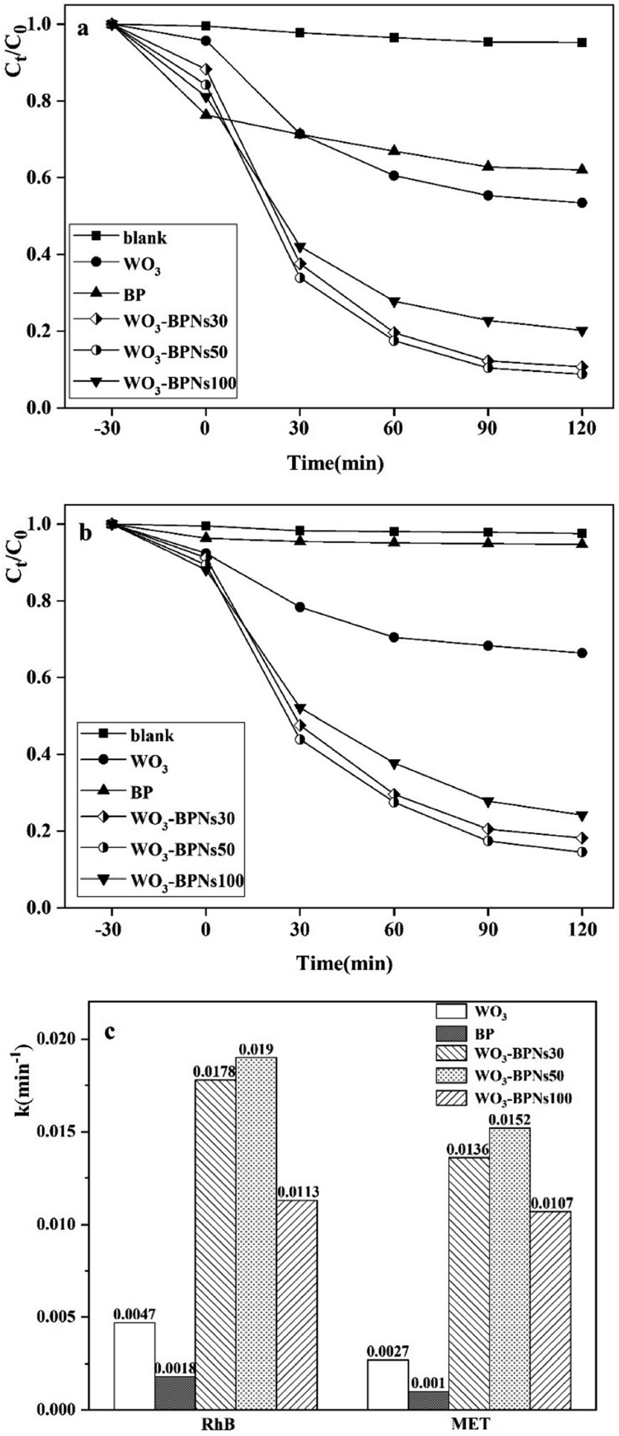

Fig. 8 Photocatalytic degradation of RhB (a) and MET (b) using WO_3, BP and WO_3–BPNs samples. (c) First order rate constant k (min^{-1}) of all samples for RhB and MET.

length and width. The SEM image of the exfoliated BP sample exhibited the two-dimensional layered structure in Fig. 2b. Fig. 2c shows the morphology of WO_3–BPNs composites sample, where WO_3 particles were attached to the surface of BP. The SEM image confirmed the formation of WO_3–BPNs composite material between WO_3 and BPNs. Fig. 3a shows the AFM image of the prepared BPNs. The one-dimensional cross-sectional scan of the prepared BPNs surface thickness was

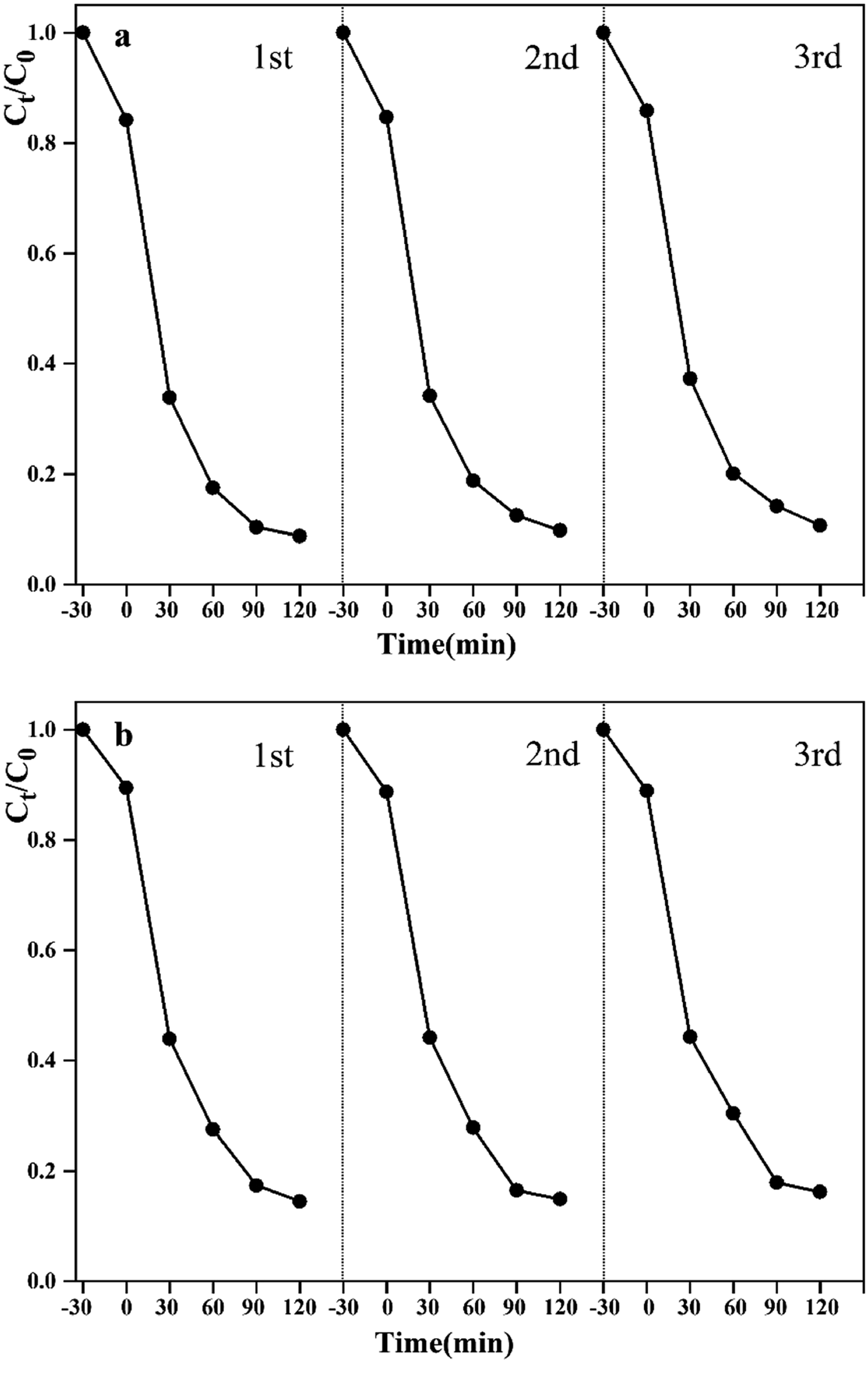

Fig. 9 Stability experiment of WO_3–BPNs50 on photocatalytic degradation of RhB (a) and MET (b) under visible-light.

shown in Fig. 3b. It could be found that the thickness of the obtained BPN was 3.2 nm. The obtained BPNs was approximately six layers of thickness due to a BP single layer of 0.53 nm.[27]

3.1.2 XPS and UV-vis analysis. The element composition and valence of the WO_3–BPNs samples were analyzed with XPS. The XPS spectra for W 4f, O 1s and P 2p of the all samples are listed in Fig. 4. There were two strong characteristic peaks ascribed to the binding energies for W $4f_{7/2}$ and W $4f_{5/2}$ in Fig. 4a. The binding energy of W $4f_{7/2}$ and W $4f_{5/2}$ were measured at 35.6 eV and 37.7 eV, respectively, which were following the previous reports.[5] The two peaks of both W $4f_{7/2}$ and W $4f_{5/2}$ for WO_3–BPNs were shifted by 0.2 eV towards lower energy compared with those of WO_3, as presented in Fig. 4a(1) and (2). The O 1s XPS spectra of WO_3 and WO_3–BPNs are shown in Fig. 4b. The peaks at 530.4 eV and 530.2 eV corresponded to the O^{2-} ion in the W–O bond of WO_3 and WO_3–BPNs, respectively. It can be found that the peak of O 1s for WO_3–BPNs shifted to the low energy of 530.2 eV, which was related to the adsorbed oxygen at the sample surface.[9,23] Fig. 4c presents, three peaks of BPNs detected at 129.2 eV, 130.2 eV and 134.2 eV, which were attributed to the P $2p_{3/2}$, P $2p_{1/2}$, and oxidized phosphorus (P_xO_y), respectively.[28] The two characteristic peaks of P $2p_{1/2}$ and P $2p_{2/3}$ of WO_3–BPNs shifted to the higher binding energy of 130.3 eV and 129.6 eV, respectively, while the binding energy of P_xO_y decreased to 132.9 eV.

The change in binding energy in the composite means that there was a close interaction between WO_3 and BPNs.[23] In the composite material, the binding energy of O 1s decreased and the binding energy of P 2p increased, suggesting the interaction between WO_3 and BPNs in the WO_3–BPNs composites.[28] The WO_3–BPNs composite showed a P 2p binding energy at 133.6 eV, suggesting that phosphorus in the composites existed in the form of a pentavalent oxidation state, and was obviously in the form of a P–O bond.[23] In addition, XPS analysis showed that phosphorus ions on the surface of WO_3–BPNs were in the states of P^{5+} and P^{3+}, which provided direct evidence for the electronic transfer between WO_3 and BPNs.

The absorption edge was affected by the bandgap width of the photocatalyst, which determined the light absorption region of the sample.[29] Fig. 5a exhibits the UV-vis absorption spectra of WO_3, BPNs and WO_3–BPNs samples. The absorption value of BPNs in different wavelength ranges did not change significantly, and the absorption value of BPNs was much higher than that of WO_3 in the visible range. The presence of BPNs enhanced the light absorption significantly for the WO_3–BPNs sample in the region of wavelength $\lambda > 400$ nm. Such an effect generally increased with the increase of the amount of BPNs. The reason was that BP could absorb a wide range of radiation from visible to infrared light because the bandgap energy of BP depended on the thickness.[21] Fig. 5b shows the calculation of bandgap energy of WO_3 and the WO_3–BPNs by Tauc equation.[8] The results show that the calculated bandgap energy of the WO_3–BPNs50 and WO_3 was 2.2 eV and 2.5 eV, respectively. However, BPNs belonged to black crystals and the calculated bandgap energy could not obtained be by diffuse reflection spectroscopy. The bandgap energy of BPNs depended on its thickness. AFM results showed that the thickness of BPNs was about 6 layers of nanosheets. According to the theoretical calculation method reported previously,[30] the bandgap energy of the BPNs was about 0.5 eV.

The XPS valence band spectrum shows that the valence band edge potentials (E_{VB}) of WO_3, BPNs and WO_3–BPNs50 are 3.14, 1.24 and 2.51 eV, as shown in Fig. 5c. The valence band edge potential (E_{VB}) of WO_3–BPNs50 was shifted to a lower energy by 0.63 eV compared to that of WO_3. According to the bandgap energy and empirical formulas ($E_{VB} = E_{CB} + E_g$), the conduction band edge potentials (E_{CB}) of WO_3, BPNs and WO_3–BPNs were 0.63, 0.74 and 0.31 eV respectively. The reduction of the WO_3–BPNs50 bandgap energy could broaden the spectral response range and be photoexcited by long-wavelength light.

3.1.3 Adsorption experiment and specific surface aperture analysis (BET). The adsorption capacity of the WO_3–BPNs sample was studied by adsorption experiment and specific surface pore size analysis. As shown in Fig. 6a, the adsorption of RhB and MET by the samples mainly occurred in the first 10 minutes, and the subsequent adsorption gradually became gentle and reached equilibrium within 30 minutes. The WO_3–BPNs sample had a relatively strong adsorption capacity for RhB and the maximum adsorption capacity was 19.8%, while the maximum adsorption for MET was only 11.8%. The adsorption capacity of WO_3–BPNs sample for RhB increased with the increased of BPNs doping amount in the composite sample. However, the photosensitization phenomenon occurred on the RhB surface under visible light, and a large amount of RhB adsorbed on the catalyst surface may have a negative impact on the degradation performance.[31]

Fig. 7 shows the nitrogen absorption–desorption isotherms and corresponding pore size distribution curves of WO_3 and WO_3–BPNs50 sample. The adsorption and desorption isotherms of WO_3 and WO_3–BPNs50 sample were all of type IV, and there was a sharp rise at the relative pressure of about 0.9 Pa. In addition, there was no obvious difference in the pore size

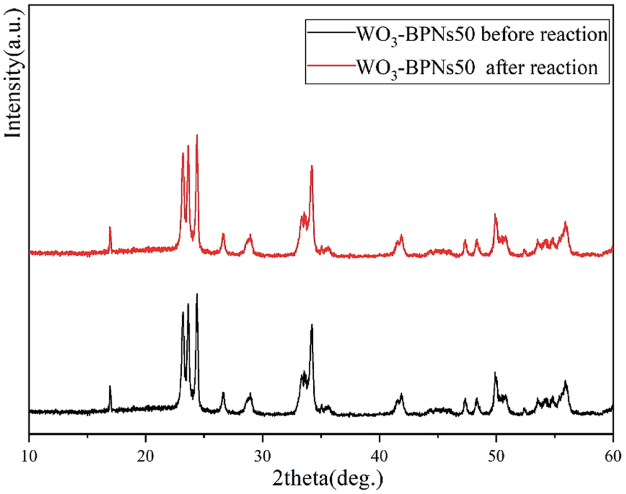

Fig. 10 XRD patterns of the WO_3–BPNs50 sample before reaction and after photocatalytic reaction under visible-light.

distribution of WO_3 and WO_3–BPNs50 sample. The BET analysis results showed that the specific surface area of WO_3 and WO_3–BPNs50 samples were 13.97 and 10.50 $m^2\ g^{-1}$, respectively. The specific surface area of WO_3–BPNs50 sample was lower than that of WO_3 due to the presence of BPNs.

3.2 Photocatalytic activities study

All samples were examined for photocatalytic activity by photodegrading RhB and MET solutions under visible-light. The photocatalytic activities of RhB and MET for all samples (WO_3, BP, and various amounts (mL) of BPNs dispersion in WO_3–BPNs composites) are presented in Fig. 8a and b. It can be observed that the photodegradation performance was optimal when the dispersion amount of BPNs was 50 mL. As observed in Fig. 8a, 92% RhB was photodegraded by WO_3–BPNs50 composite material within 120 minutes, while only 47% reduction was achieved by pure WO_3. Similarly, 87% MET was photodegraded by WO_3–BPNs composite material, while it was only 37% by pure WO_3, as shown in Fig. 8b. More doping of BPNs (WO_3–BPNs100) decreased the photocatalytic efficiency compared with the WO_3–BPNs50 sample. Excessive BPNs will stimulate more photo-generated holes on the surface of BPNs. The results of VBXPS tests indicated that the valence band edge potential of BPNs was only 1.24 eV, and the oxidation ability of

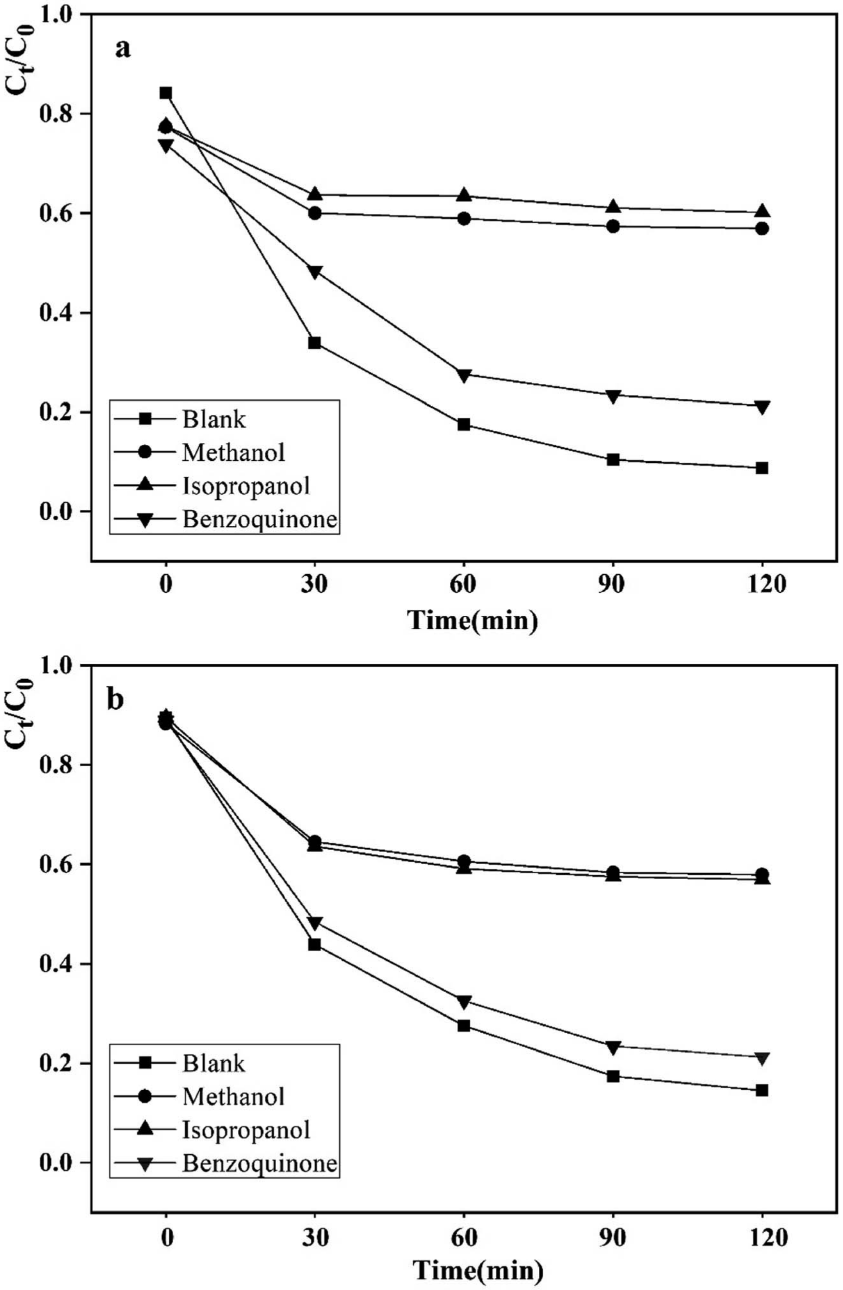

Fig. 11 Effects of radical scavengers on the performance of the WO_3–BPNs50 in degrading RhB (a) and MET (b).

photogenerated holes (h^+) on the surface of BPNs was consequently poor.

The first-order rate constants k (min^{-1}) of photodegradation RhB and MET of all samples were calculated by the first-order equation,[32] as shown in Fig. 8c.

$$\ln(C_0/C) = kt \tag{1}$$

where C_0 is the initial concentration of RhB and MET, and C is the concentration of the solution at time t. During the photodegradation of RhB and MET, the maximum values of the first-order reaction rate constants k were 0.019 and 0.0152 min^{-1} respectively, corresponding to the WO_3–BPNs50 sample.

The recycling experiments were conducted to explore the stability of the synthesized WO_3–BPNs50 composite under visible-light. The photocatalyst WO_3–BPNs50 was recovered by centrifugation after each trial, and a recycling test was performed under the same conditions as in the photodegradation experiment of RhB and MET described above. As shown in Fig. 9, WO_3–BPNs50 could still maintain 97.9% and 97.4% degradation performance of RhB and MET after three cycles of experiments compared with their first photodegradation results. In addition, the X-ray diffraction pattern confirmed that there was no change in the structure of the sample before and after the photocatalytic reaction in Fig. 10. These indicate that the WO_3–BPNs50 composite had high stability after the photocatalytic reaction.

3.3 The photocatalytic mechanisms of WO_3–BPNs

The photocatalytic species capture experiment was carried out under visible-light. Methanol, *p*-benzoquinone and isopropanol were selected as scavengers for the holes (h^+), superoxide radicals ($\cdot O^{2-}$), and hydroxyl radicals ($\cdot OH$) respectively in degrading RhB and MET.[8] It can be observed that the photodegradation performance of the WO_3–BPNs composite was not significantly inhibited by adding *p*-benzoquinone, while that was inhibited after adding methanol and isopropanol in Fig. 11a and b. The results suggested that the h^+ and $\cdot OH$ were the main active species during the photodegradation of RhB and MET.

The photocatalytic degradation mechanism of the WO_3–BPNs composite is schematically described in Fig. 12. Photogenerated electron–hole pairs will be produced inside the semiconductor as light is irradiated on the surface of the WO_3–BPNs composite. The photogenerated electrons (e^-) in the conduction band of WO_3 were transferred to the surface of BPNs, because the conduction band edge potential of BPNs (0.74 eV) was higher than WO_3 (0.64 eV).[28] However, the photogenerated holes (h^+) in the WO_3 valence band were difficult to transfer to the surface of the BPNs since the valence band edge potential of the WO_3 (3.14 eV) was much higher than that of BPNs (1.24 eV), resulting in a longer photogenerated hole (h^+) transfer path. Photogenerated holes (h^+) on the surface of BPNs cannot oxidize OH^- to form $\cdot OH$ radicals ($E_{OH^-/\cdot OH} = 2.4$ eV *vs.* NHE).[33] Therefore, photogenerated holes (h^+) on the surface of WO_3 played a major role to oxidize OH^- to form $\cdot OH$ radicals, which could further oxidize RhB and MET. In addition, the photo-generated electrons (e^-) on the conduction band of BPNs and WO_3 could not react with O_2 to generate $\cdot O^{2-}$ radicals, because the redox potential of O_2 to $\cdot O^{2-}$ (−0.33 eV *vs.* NHE) was lower than the conduction edge potential of BPNs (0.74 eV) and WO_3 (0.64 eV).[34] $\cdot O^{2-}$ radicals were not the main active species of photodegradation reaction of RhB and MET, corresponding to the results of the active species capture experiment.

The photo-generation of electrons and holes mainly depends on the absorption of light energy higher than the bandgap energy of the semiconductor material, and the lower bandgap energy is more likely to stimulate the generation of photogenerated electron–hole pairs and improve photocatalytic activity.[9] The calculated bandgap energy of WO_3–BPNs50 and WO_3 was 2.2 eV and 2.5 eV, respectively. The valence band edge potential (E_{VB}) and calculated band gap energy of the WO_3–BPNs50 sample were lower than those of WO_3, which could broaden the spectral response range and be photoexcited by long-wavelength light. Moreover, BPNs in the WO_3–BPNs50 heterojunction acted as a co-catalyst to receive and transfer photogenerated electrons in the photocatalytic reaction process, which effectively reduced the recombination of photogenerated electron–hole pairs and significantly enhanced the photocatalytic performance.[23] The XPS results suggested that the electron density increased and decreased in WO_3 and BPNs, which also explained the transfer of electrons in the WO_3–BPNs composite. Therefore, the reason for improving photocatalytic performance of the WO_3–BPNs composite was majorly attributed the lower optical bandgap energy and BPNs as a co-catalyst in the WO_3–BPNs heterojunction.

3.4 Degradation pathways and intermediates of MET

The toxic and harmful intermediate products may be generated during the degradation of organic pollutants.[35,36] MET, unlike industrial dyes (RhB), is widely used in both hospitals and households, which eventually enters surface waters, including drinking water sources. Therefore, the identification of MET degradation intermediates is significantly for ensuring the

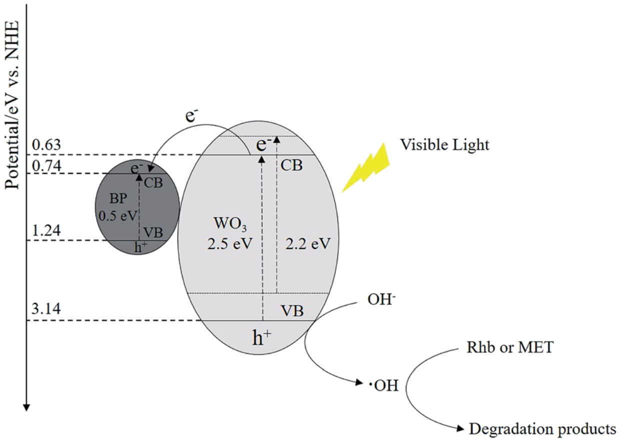

Fig. 12 Schematic photodegradation mechanism of the synthesized WO_3–BPNs.

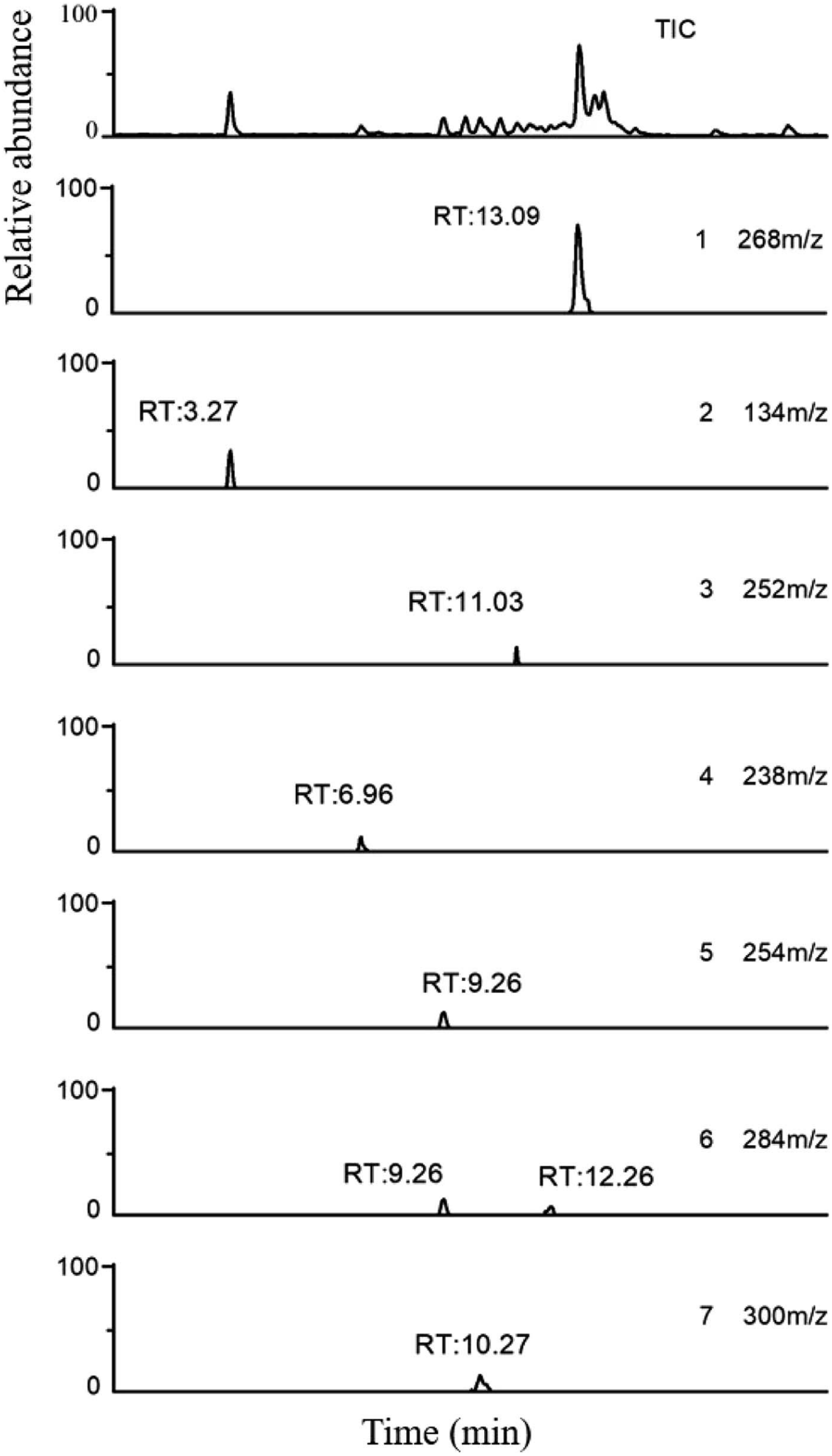

Fig. 13 LC-MS total ion chromatogram (TIC) and extracted ions chromatograms of MET (**1**) and its intermediates (**2–7**) using WO_3–BPNs.

safety of water supply. In this study, LC-MS technology was used to detect and identify potential MET intermediates.

As shown in Fig. 13, the chromatograms of total ion (TIC), MET, and six intermediates were obtained with LC-MS at unequal retention times. The mass-to-charge ratios (*m*/*z*) of these seven compounds were 268, 134, 252, 238, 254, 284, and 300 *m*/*z*, respectively. Combined with the structural characteristics of the MET molecule, the structures of the six

Table 1 Proposed structures of the intermediates for the photocatalytic degradation of MET using WO_3–BPNs

Compound	Molecular formula	$[M + H]^+$ m/z	Structural formula
1	$C_{15}H_{25}NO_3$	268	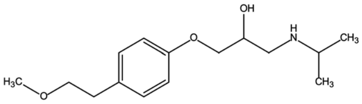
2	$C_6H_{15}NO_2$	134	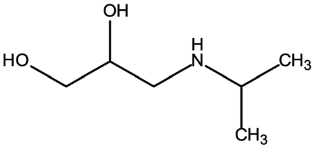
3	$C_{14}H_{21}NO_3$	252	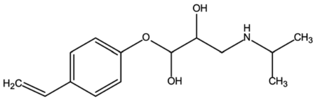
4	$C_{13}H_{19}NO_3$	238	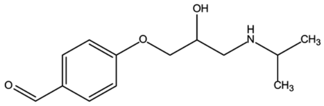
5	$C_{13}H_{19}NO_4$	254	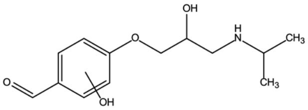
6	$C_{15}H_{25}NO_4$	284	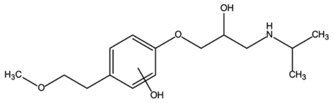
7	$C_{15}H_{25}NO_5$	300	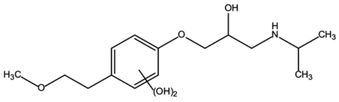

intermediates were identified (Table 1). The photocatalytic degradation pathway for MET was proposed according to the determination of MET intermediates and the photodegradation mechanism of the WO_3–BPNs composites in Fig. 14.

First, the MET molecule (**1**) was attacked by the ·OH radical, which caused the broken of the C–C bond in the aliphatic portion of the MET molecule and the producing amino-diol (**2**) intermediates.[37,38] The corresponding phenol produced by MET

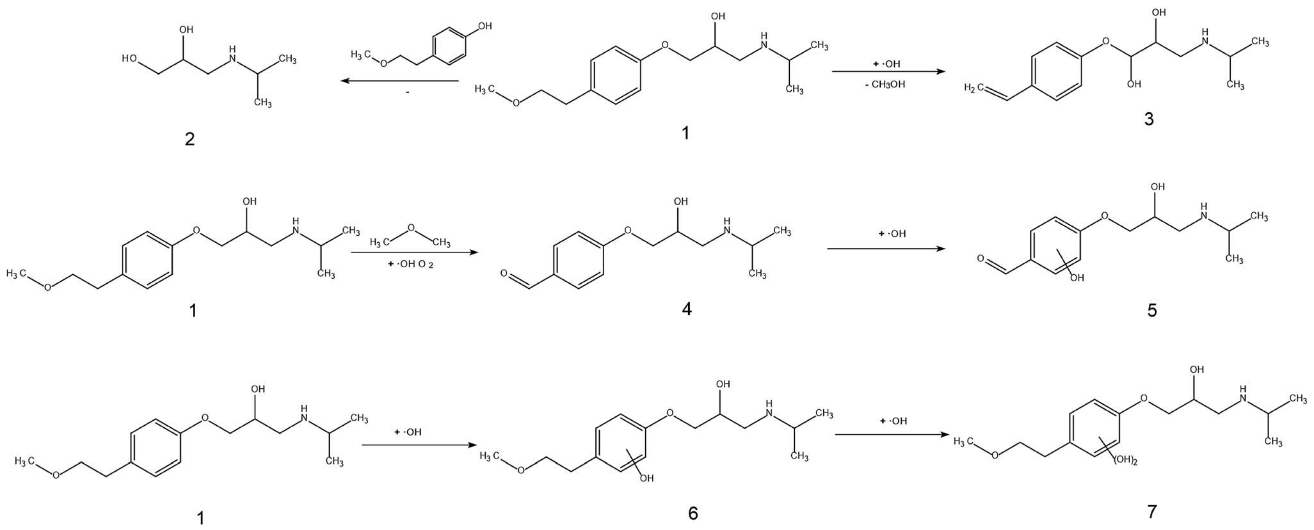

Fig. 14 Tentative pathways for the photocatalytic degradation of MET using WO_3–BPNs.

was also intermediate.[39] Intermediate (**3**) may be formed due to the oxidation of ·OH radicals in the aliphatic part of MET to C atoms near ether oxygen and the loss of methanol, which formed a characteristic peak at the retention time of 11.03 minutes (Fig. 11). Second, intermediate (**4**) and (**5**) with 238 and 254 *m*/*z* were identified from the peaks formed at the retention time of 6.96 minutes and 9.26 minutes, respectively, in Fig. 11. The combine O-atom addition and the loss of ether group, owing to ·OH attacking the alkyl group, led to form intermediate (**4**). Intermediate (**5**) could be formed by the attack of ·OH on the aromatic ring of intermediate (**4**).[39] Intermediate (**4**) had two substituents on the aromatic ring, in which the –CHO substituent had a *meta*-orientating character and electron-withdrawing, and the other substituent was *ortho*/*para* orientating character and an alkoxy group with an electron-donating.[40] Therefore, ·OH was more conducive to attack the *meta* position of –CHO group under the combined action of two substituents, forming the intermediate (**5**). In addition, the mono-hydroxylated intermediate (**6**) with 284 *m*/*z* and the di-hydroxylated intermediate **7** with 300 *m*/*z* was identified, which was also caused by the ·OH radical attack on the benzene ring of the MET molecule.

4 Conclusion

The WO_3–BPNs heterojunction composite was successfully prepared using a combined hydrothermal, liquid phase exfoliating and co-precipitation method. The as-obtained WO_3–BPNs composite was characterized by using XRD, SEM, AFM, XPS, BET and UV-vis. The results showed that the valence band edge potential of the WO_3–BPNs50 was shifted to a lower energy and the bandgap energy of the WO_3–BPNs50 was lower than that of WO_3, which could broaden the spectral response range and be photoexcited by long-wavelength light. The WO_3–BPNs sample exhibited promoted photocatalytic activity in photo-degrading RhB and MET as comparison with pure WO_3 and BPNs under visible-light. The maximum RhB and MET removal efficiency were achieved at 92% and 87% for the WO_3–BPNs50 sample within 120 minutes. Three cycles of experiments and XRD measurements of the samples before and after photodegradation suggested the excellent stability of the WO_3–BPNs50 sample. The photodegradation mechanisms of the WO_3–BPNs composite were also proposed. BPNs in WO_3–BPNs50 heterojunction acted as a co-catalyst to receive and transfer photogenerated electrons in the photocatalytic reaction process, which effectively reduced the recombination of photogenerated electron–hole pairs and significantly enhanced the photocatalytic performance. Finally, six intermediates in the MET photodegradation process were detected by LC-MS, and the tentative pathways were proposed for the photo-degradation of MET.

Conflicts of interest

There are no conflicts to declare.

Acknowledgements

The work was supported by the National Natural Science Foundation of China (No. 41771502).

References

1 L. Jianga, X. Yuana, G. Zenga, Z. Wua and L. Jie, Metal-free efficient photocatalyst for stable visible-light photocatalytic degradation of refractory pollutant, *Appl. Catal., B*, 2017, **221**, 715–725.

2 A. Fujishima and K. Honda, Electrochemical Photolysis of Water at a Semiconductor Electrode, *Nature*, 1972, **238**, 37–38.

3 A. Mills and S. L. Hunte, An Overview of Semiconductor Photocatalysis, *J. Photochem. Photobiol., A*, 1997, **108**, 1–35.

4 D. Jiang, S. Zhang and H. Zhao, Photocatalytic Degradation Characteristics of Different Organic Compounds at TiO_2 Nanoporous Film Electrodes with Mixed Anatase/Rutile Phases, *Environ. Sci. Technol.*, 2007, **41**, 303–308.

5 F. Han, H. Li, F. Li, J. Yang and L. Zhong, Synthesis of S-doped WO_3 nanowires with enhanced photocatalytic performance towards dye degradation, *Chem. Phys. Lett.*, 2016, **651**, 183–187.

6 X. Zhang, *et al.*, Effect of aspect ratio and surface defects on the photocatalytic activity of ZnO nanorods, *Sci. Rep.*, 2014, **4**, 4596.

7 L. Mao, X. Cai, S. Yang, K. Han and J. Zhang, Black phosphorus-CdS-$La_2Ti_2O_7$ ternary composite: effective noble metal-free photocatalyst for full solar spectrum activated H_2 production, *Appl. Catal., B*, 2018, **242**, 441–448.

8 L. Gao, *et al.*, Preparation of heterostructured WO_3/TiO_2 catalysts from wood fibers and its versatile photodegradation abilities, *Sci. Rep.*, 2017, **7**, 1102.

9 R. Asahi, T. Morikawa, T. Ohwaki, K. Aoki and Y. Taga, Visible-light photocatalysis in nitrogen-doped titanium oxides, *Science*, 2001, **293**, 269–271.

10 Q. Shi, D. Yang, Z. Jiang and J. Li, Visible-light photocatalytic regeneration of NADH using P-doped TiO_2 nanoparticles, *J. Mol. Catal. B: Enzym.*, 2006, **43**, 44–48.

11 A. Garzon-Roman, C. Zuñiga-Islas and E. Quiroga-González, Immobilization of doped TiO_2 nanostructures with Cu or In inside of macroporous silicon using the solvothermal method: morphological, structural, optical and functional properties, *Ceram. Int.*, 2020, **46**, 1137–1147.

12 C. S. Park, V. R. Shrestha, S. S. Lee, E. S. Kim and D. Y. Choi, Omnidirectional color filters capitalizing on a nano-resonator of Ag-TiO_2-Ag integrated with a phase compensating dielectric overlay, *Sci. Rep.*, 2015, **5**, 8467.

13 W. Liang, L. Jian and Y. Jin, Photo-catalytic degradation of gaseous formaldehyde by TiO_2/UV, Ag/TiO_2/UV and Ce/TiO_2/UV, *Build. Environ.*, 2012, **51**, 345–350.

14 E. S. Reich, Phosphorene excites materials scientists, *Nature*, 2014, **506**, 19.

15 M. H. H. Ali, A. D. Al-Afify and M. E. Goher, Preparation and characterization of graphene-TiO_2 nanocomposite for

enhanced photodegradation of rhodamine-B dye, *Egypt. J. Aquat. Res.*, 2018, **44**, 263–270.

16 S. Kanda, *et al.*, Facile synthesis and catalytic activity of MoS_2/TiO_2 by a photodeposition-based technique and its oxidized derivative MoO_3/TiO_2 with a unique photochromism, *J. Colloid Interface Sci.*, 2011, **354**(2), 607–610.

17 L. Liao, *et al.*, High-speed graphene transistors with a self-aligned nanowire gate, *Nature*, 2010, **467**, 305–308.

18 B. Radisavljevic, A. Radenovic, J. Brivio, V. Giacometti and A. Kis, Single-layer MoS_2 transistors, *Nat. Nanotechnol.*, 2011, **6**, 147–150.

19 F. Xia, H. Wang and Y. Jia, Rediscovering black phosphorus as an anisotropic layered material for optoelectronics and electronics, *Nat. Commun.*, 2014, **5**, 4458.

20 J. Qiao, X. Kong, Z. X. Hu, F. Yang and W. Ji, High-mobility transport anisotropy and linear dichroism in few-layer black phosphorus, *Nat. Commun.*, 2014, **5**, 4475.

21 D. J. Perello, S. H. Chae, S. Song and Y. H. Lee, High-performance n-type black phosphorus transistors with type control via thickness and contact-metal engineering, *Nat. Commun.*, 2015, **6**, 7809.

22 L. Li, *et al.*, Black phosphorus field-effect transistors, *Nat. Nanotechnol.*, 2014, **9**, 372–377.

23 H. Uk Lee, *et al.*, Stable semiconductor black phosphorus (BP)@titanium dioxide (TiO_2) hybrid photocatalysts, *Sci. Rep.*, 2015, **5**, 8691.

24 J. Hu, *et al.*, Z-Scheme 2D/2D Heterojunction of Black Phosphorus/Monolayer Bi_2WO_6 Nanosheets with Enhanced Photocatalytic Activities, *Angew. Chem.*, 2019, **131**, 2095–2099.

25 M. Zhu, X. Cai, M. Fujitsuka, J. Zhang and T. Majima, Au/$La_2Ti_2O_7$ Nanostructures Sensitized with Black Phosphorus for Plasmon-Enhanced Photocatalytic Hydrogen Production in Visible and Near-Infrared Light, *Angew. Chem., Int. Ed.*, 2017, **56**, 2064.

26 Z. Ying, D. Zhang, X. Xu and B. Zhang, Morphology control and photocatalytic characterization of WO_3 nanofiber bundles, *Chin. Chem. Lett.*, 2018, **29**, 40–44.

27 P. Yasaei, *et al.*, High-quality black phosphorus atomic layers by liquid-phase exfoliation, *Adv. Mater.*, 2015, **27**, 1887–1892.

28 M. Zhu, C. Zhai, M. Fujitsuka and T. Majima, Noble Metal-Free Near-Infrared-Driven Photocatalyst for Hydrogen Production Based on 2D Hybrid of Black Phosphorus/WS_2, *Appl. Catal., B*, 2017, **221**, 645–651.

29 G. Carbajal-Franco, M. Eastman and C. V. Ramana, Structure and optical properties of iron oxide films prepared by a modified wet-chemical method, *Ceram. Int.*, 2013, **39**, 4581–4587.

30 T. Sakthivel, X. Y. Huang, Y. C. Wu and S. Rtimi, Recent progress in black phosphorus nanostructures as environmental photocatalysts, *Chem. Eng. J.*, 2020, **379**, 122297.

31 J.-M. Wu and T.-W. Zhang, Photodegradation of rhodamine B in water assisted by titania films prepared through a novel procedure, *J. Photochem. Photobiol., A*, 2004, **162**, 171–177.

32 Y. Xu, W. Wen and J. M. Wu, Titania nanowires functionalized polyester fabrics with enhanced photocatalytic and antibacterial performances, *J. Hazard. Mater.*, 2018, **343**, 285–297.

33 S. Meng, J. Zhang, S. Chen, S. Zhang and W. Huang, Perspective on construction of heterojunction photocatalysts and the complete utilization of photogenerated charge carriers, *Appl. Surf. Sci.*, 2019, **476**, 982–992.

34 M. J. Islam, *et al.*, An oxygen-vacancy rich 3D novel hierarchical MoS_2/BiOI/AgI ternary nanocomposite: enhanced photocatalytic activity through photogenerated electron shuttling in a Z-scheme manner, *Phys. Chem. Chem. Phys.*, 2016, **18**, 24984–24993.

35 X. Cai, J. Ye, G. Sheng and W. Liu, Time-dependent degradation and toxicity of diclofop-methyl in algal suspensions: emerging contaminants, *Environ. Sci. Pollut. Res. Int.*, 2009, **16**, 459–465.

36 H. Li, Y. Yuan, C. Shen, Y. Wen and H. Liu, Enantioselectivity in toxicity and degradation of dichlorprop-methyl in algal cultures, *J. Environ. Sci. Health, Part B*, 2008, **43**, 288–292.

37 H. Yang, *et al.*, Photocatalytic degradation kinetics and mechanism of environmental pharmaceuticals in aqueous suspension of TiO_2: a case of beta-blockers, *J. Hazard. Mater.*, 2010, **179**, 834–839.

38 V. Romero, *et al.*, Photocatalytic treatment of metoprolol and propranolol, *Catal. Today*, 2011, **161**, 115–120.

39 B. Abramovic, *et al.*, Photocatalytic degradation of metoprolol tartrate in suspensions of two TiO_2-based photocatalysts with different surface area. Identification of intermediates and proposal of degradation pathways, *J. Hazard. Mater.*, 2011, **198**, 123–132.

40 M. M. Huber, S. Canonica, G. Y. Park and U. von Gunten, Oxidation of pharmaceuticals during ozonation and advanced oxidation processes, *Environ. Sci. Technol.*, 2003, **37**, 1016–1024.